Defects production and mechanical properties of typical metal engineering materials under neutron irradiation

LIU Jian[1], TANG XiaoBin[1,2*], CHEN FeiDa[1], HUANG Hai[1], LI Huan[1] & YANG YaHui[1]

[1]*Department of Nuclear Science & Engineering, Nanjing University of Aeronautics and Astronautics, Nanjing 210016, China;*
[2]*Jiangsu Key Laboratory of Nuclear Energy Equipment Materials Engineering, Nanjing 210016, China*

Maintaining the safety and reliability of nuclear engineering materials under a neutron irradiation environment is significant. Atomic-scale simulations are conducted to investigate the mechanism of irradiation-induced vacancy formation in CLAM, F82H and α-Fe with different neutron energies and objective laws of the effect of vacancy concentration on mechanical properties of α-Fe. Damage of these typical metal engineering materials caused by neutrons is mainly displacement damage, while the displacement damage rate and the non-ionizing effect of neutrons decrease with the increase of neutron energy. The elastic modulus, yield strength, and ultimate strength of α-Fe are in the order of magnitude of GPa. However, the elastic modulus is not constant but decreases with the increase of strain at the elastic deformation stage. The ultimate strength reaches its maximum value when vacancy concentration in α-Fe is 0.2%. On this basis, decreasing or increasing the number of vacancies reduces the ultimate strength.

1   Introduction

Materials in reactors are associated with safe operation of nuclear power plants [1,2]. With the rapid development of modern nuclear power systems, harsh working conditions, including high operation temperature and increasing neutron flux, have raised the irradiation tolerance requirements for engineering materials used in reactors [3–7]. A large amount of research focusing on new materials has been conducted to meet the aforementioned requirements [8]. However, the breakthrough in new materials requires a profound understanding of the mechanism of material microscopic damage formation. Therefore, studying the failure and destruction of metals at atomic scale under high tem-

perature, high pressure, and strong irradiation within the reactors, which assures the life span of the reactor, is significant. An earlier study observed that neutron irradiation causes degradation of metal performance through radiation-induced hardening and embrittlement at low temperature [9,10], element segregation [11], creep [12], swelling [13], and helium-induced embrittlement [14] at high temperature, which pose a security risk to nuclear power plant operations.

The most obvious way to investigate the effect of irradiation damage to the materials is to perform irradiation experiments to explore the variation of macroscopic properties and microstructure of the specific material before and after irradiation. The limitations of experimental technique cause difficulty in controlling the experimental conditions and achieving accurate measurements. Specifically, the most

*Corresponding author (email: tangxiaobin@nuaa.edu.cn)

effective way to explore the microscopic mechanism of irradiation damage of certain materials at atomic scale is to perform computer simulation. With the development of computer technology and theoretical basis of computer simulation, the mechanism of material irradiation damage has been revealed. Barashenkov presented Monte Carlo simulations of ionization and nuclear processes initiated by hadron and ion beams [15]. Osetsky et al. [17] employed molecular dynamics (MD) method to research the formation of extended defect clusters [16] and stability and mobility of defect clusters in α-Fe and Cu. A combination of MD and kinetic Monte Carlo (kMC) methods was taken by Caturla et al. [18] to investigate radiation damage evolution. Thus, computer simulation has become an important part of solving practical problems in material science.

However, the mechanism of damage formation in specific materials used in reactors at present is still unrevealed. In this paper, the microscopic mechanism of damage of interaction between neutrons and structural materials in the reactor, as well as the mechanical properties after neutron irradiation, is studied. In this study, Monte Carlo method is employed to examine the mechanism of irradiation damage of CLAM steel, F82H steel, and α-Fe, which are widely used as structural materials in reactors, under bombardment of neutrons with energy of 2.45 and 14.1 MeV. Then, molecular dynamics method is used to study the stress-strain curve, elastic modulus, and ultimate strength of α-Fe after neutron irradiation, during which the irradiation-induced vacancies remain in the bulk α-Fe.

2 Simulation model

2.1 Monte Carlo model

Monte Carlo simulation software Geant4 is employed to study the mechanism of irradiation damage [19]. Figure 1 shows the geometric model that consists of three parts: the world part, the target part, and the sensitive detector part. The world part is a cube with a length of 450 mm. The target part, a cuboid with size of 400 mm × 320 mm × 320 mm, is filled with CLAM steel, F82H steel, or α-Fe. As shown in Table 1, the elementary composition of these three materials is different. The sensitive detector part is made up of 20000 cuboid films with a size of 0.02 mm × 300 mm × 300 mm. In other words, the sensitive detector part divides the target part into 20000 pieces along the direction of incident neutrons. Thus, this part can gain the damage effect of the whole target by recording the information obtained on every single film.

The direction of incident neutrons is [100], which is perpendicular to the surface of the target, and the incident dots distribute uniformly on the surface. The energy of neutrons is 2.45 and 14.1 MeV, respectively. According to the deposition energy obtained by detectors, defect number can be
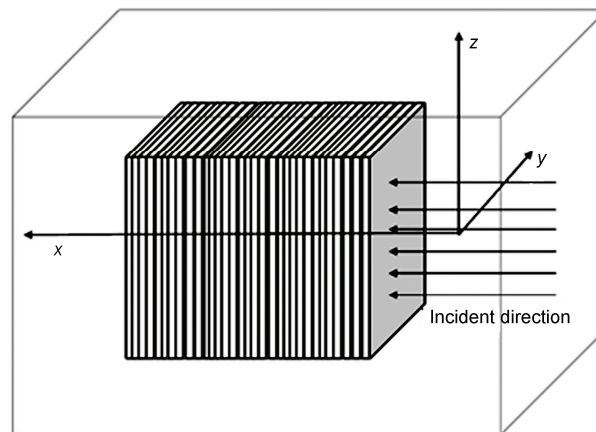

Figure 1 Geometric model of Monte Carlo simulation.

Table 1 Parameters of three different target materials

Element	Molar mass (g/mol)	Mass fraction (%)		
		CLAM	F82H	α-Fe
Fe	55.847	88.69	90.01	100
Cr	51.996	9.0	7.46	0
C	12.011	0.12	0.9	0
Mn	54.938	0.5	0.21	0
P	30.973	0.03	0	0
S	32.061	0.02	0	0
N	14.006	0.02	0	0
W	183.85	1.6	2.23	0
Ni	58.701	0.02	0	0

calculated as

$$N_d(E) = \begin{cases} 0, & E < E_d, \\ 1, & E_d \leqslant E < 2.5E_d, \\ 0.4E_D(E)/E_d, & E \geqslant 2.5E_d, \end{cases} \quad (1)$$

where N_d is defect number, E is energy of primary knockout atom, E_d is displacement energy threshold, and $E_D(E)$ is the energy available to generate atomic displacements, which can be determined by

$$E_D(E) = \frac{E}{1 + kg(\varepsilon)}, \quad (2)$$

$$\varepsilon = \frac{E}{30.724Z_1Z_2\sqrt{Z_1^{2/3} + Z_2^{2/3}}\left(1 + \dfrac{A_1}{A_2}\right)}, \quad (3)$$

$$g(\varepsilon) = 3.4008\varepsilon^{1/6} + 0.40244\varepsilon^{3/4} + \varepsilon, \quad (4)$$

$$k = 0.1337Z_1^{1/6}\left(Z_1/A_1\right)^{1/2}, \quad (5)$$

where Z_1 and Z_2 are the atomic numbers of the projectile and target and A_1 and A_2 are the mass numbers of the two atoms [20,21]. Then we could use defect number to get the displacement per atom (DPA) and displacement damage

rate (DDR). In this paper, we calculated DDR at a neutron fluence of 1/1024 n/cm^2 since only one neutron hit the target part at a single time.

2.2   Molecular dynamics model

In this paper, the Finnis–Sinclair potential [22] is used to describe the interaction of Fe atoms, which is expressed as

$$E = \frac{1}{2}\sum_{i \neq j=1}^{N} V_{ij}\left(x_{ij}\right) - \sum_{i=1}^{N}\left(\sum_{j=1}^{N} \varphi_{ij}\left(x_{ij}\right)\right)^{1/2}, \qquad (6)$$

where N is the total number of atoms in the assembly, V_{ij} is the pairwise repulsive part of the potential, and $\varphi(x_{ij})$ in the many-body, isotropic, cohesive term is also a pairwise function.

Due to the dispersion of different chemical elements in CLAM and F82H, it is very complicated to model these two kinds of steel. Thus, we investigated mechanical properties of α-Fe by molecular dynamics method only. Figure 2 shows the cuboid model of α-Fe used in the molecular dynamics method before and after stretching process. The crystal structure is a body-centered cubic with a lattice constant a_0 of 0.287 nm. Containing 48000 Fe atoms, the model has length, width, and height of $60a_0$, $20a_0$, and $20a_0$, respectively. The temperature of the assembly is maintained at 300 K, which suits the room temperature [23–25]. In order to investigate the influence of vacancy concentration on material strength, atoms in the model were deleted to form vacancy by degrees of 0%, 0.1%, 0.2%, 0.5%, 1%, 2%, 5%, and 10%, respectively. A constant engineering strain rate of 1.5×10^{-2} ps^{-1} was applied to the eight models with varying vacancy concentrations, as mentioned above, along the length direction to simulate the stretching process. Meanwhile, the value of stress and strain was recorded at each step of the stretching process, which is 1 fs (1×10^{-15} s). The molecular dynamics simulations were performed using LAMMPS [26].

3   Results and discussion

3.1   DDR distribution

In this study, displacement damage rate generated in CLAM, F82H, and α-Fe by neutrons with energy of 2.45 and 14.1
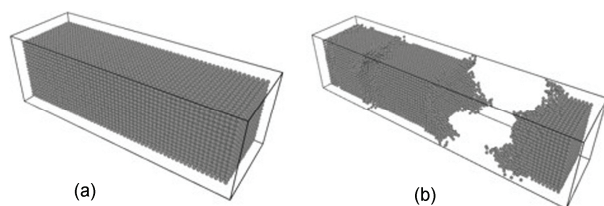

Figure 2   Geometric model of molecular dynamics simulation before (a) and after (b) stretching process.

MeV was calculated. Each simulation with various types of candidate materials and neutron energy was conducted six times, and for each simulation, the number of incident neutrons is 10^6. Figure 3 illustrates the displacement damage rate distribution that results from single neutron irradiation with different energy values in different materials.

In Figure 3(a), displacement damage rate versus incident depth is illustrated in each type of material by the 2.45 MeV neutron. According to the area enclosed by the curve and the axis, which represents total displacement damage rate, we can determine that α-Fe$_{ddr}$>F82H$_{ddr}$ $\approx$ CLAM$_{ddr}$, and the depth corresponding to the peak value of displacement damage rate in all materials is approximately 28 mm. DDR has a downward trend after rising first and decreases exponentially at the end of the curve. Notably, the maximum DDR in these three materials is 2.45×10^{-19} dpa/(n/cm^2) in α-Fe.

In Figure 3(b), we have found that α-Fe$_{ddr}$>F82H$_{ddr}$ $\approx$ CLAM$_{ddr}$ at the same depth after 14.1 MeV neutron irradiation. In these three materials, 24 mm is the depth that corresponds to the peak value of DDR, whose value is 1.86×10^{-19} dpa/(n/cm^2), 1.70×10^{-19} dpa/(n/cm^2) and 1.70×10^{-19} dpa/(n/cm^2) for α-Fe, F82H, and CLAM, respectively. Similar to the curve in Figure 3(a), the curve in Figure 3(b) also decreases after reaching the peak value.

3.2   Non-ionizing effect of neutron

Having figured out the distribution of neutron irradiation-induced DDR and with the purpose of researching the mechanism of damage formation caused by incident neutrons, we employed sensitive detectors to record DPA resulting from the non-ionizing effect of neutrons to determine the distribution of this kind of DDR with depth. The results are presented in Figures 4(a) and (b).

The findings in these two figures lead to the conclusion that neutron non-ionizing effect induced damage is almost the same in all of the three employed materials. To facilitate realizing the characteristic of damage caused by neutrons in α-Fe, we present the data in Table 2.

The depth of peak in Table 2 indicates the depth where DDR caused by the penetrating neutron reaches the maximum number, which is used to characterize the most severely damaged area. Similarly, providing the most reliable estimate of life span of a certain material, the peak of DDR indicates the maximum damage that the incident neutron can cause in it. Finally, the depth of damage demonstrates the depth of incident neutron where DDR drops to half of the peak, which can be used to represent the effective damage range of the neutron.

Table 2 shows that the non-ionizing effect of 2.45 MeV neutrons on α-Fe is ten times more than 14.1 MeV neutrons with values of 1.411×10^{-20} dpa/(n/cm^2) for the peak of DDR and 20.22 mm for the depth of peak. Based on the preceding discussion, we can speculate that the contribution of non-
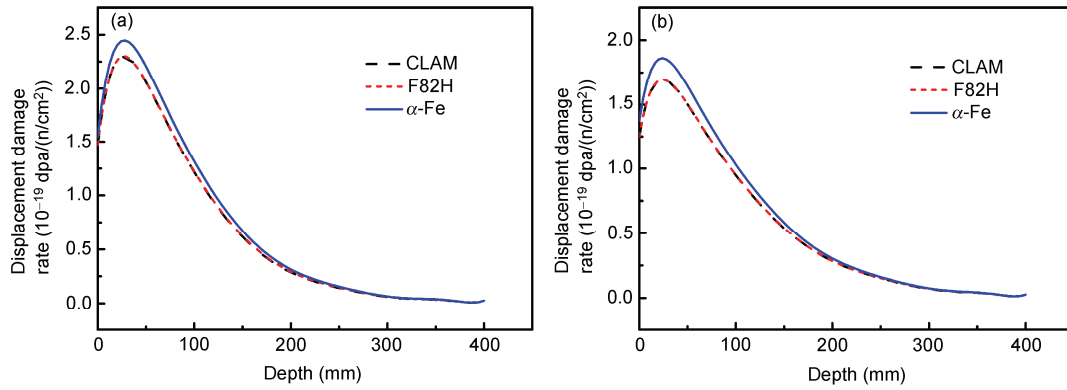
Figure 3 (Color online) (a) DDR distribution as a function of depth in three materials (CLAM, F82H, and α-Fe) after 2.45 MeV neutron irradiation, (b) DDR distribution as a function of depth in three materials (CLAM, F82H, and α-Fe) after 14.1 MeV neutron irradiation.
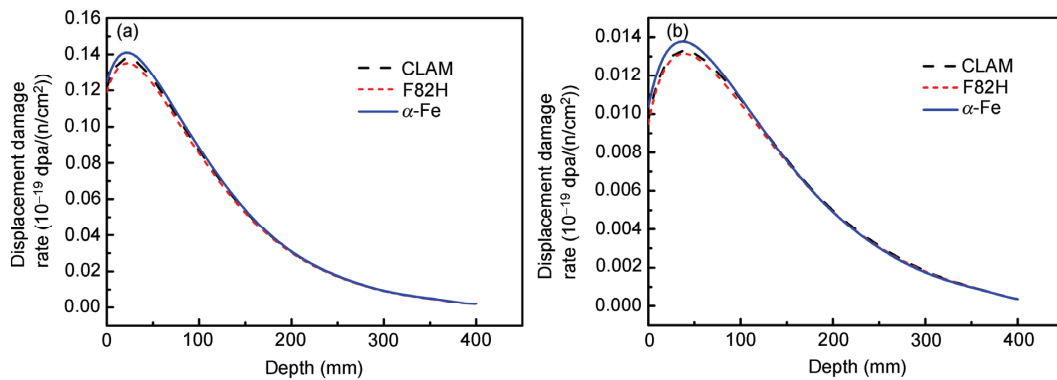

Figure 4 (Color online) (a) DDR distribution generated by non-ionizing effect of neutron as a function of depth in three materials (CLAM, F82H, and α-Fe) after 2.45 MeV neutron irradiation, (b) DDR distribution generated by non-ionizing effect of neutron as a function of depth in three materials (CLAM, F82H, and α-Fe) after 14.1 MeV neutron irradiation.

Table 2 Neutron damage data in α-Fe

Type of damage	Neutron energy (MeV)	Depth of peak (mm)	Peak of DDR (10^{-21})	Average order of magnitude of damage	Depth of damage (mm)
Total damage	2.45	28.32	244.7	10^{-19}	109
	14.1	24.28	186.1	10^{-19}	113
Non-ionizing damage	2.45	20.22	14.11	10^{-20}	125
	14.1	36.38	1.378	10^{-21}	162

ionizing damage effect is decreased with the increase of neutron energy. Nevertheless, for total damage, the peak of DDR generated by the 2.45 MeV neutron is nearly 1.31 times more than that generated by the 14.1 MeV neutron while the depth of peak and depth of damage are almost the same. Therefore, the difference in the peak of DDR results from the damage degree decreasing nonlinearly at every unit of depth after the increase in incident neutron energy.

3.3 Stress-strain curve

The stress-strain curve of perfect α-Fe (which means that it has no defect) during the stretching process is shown in Figure 5. This figure indicates that the entire stress–strain

curve is consistent with the engineering tensile stress–strain curve for plastic metals. During the tensile deformation, the model underwent elastic deformation, yield, and plastic deformation stages until it finally ruptured. Figure 6 shows the schematic corresponding to these four stages.
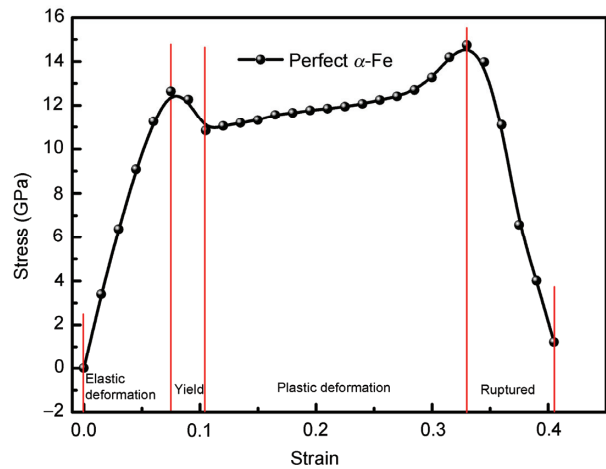
The main reason for the phenomenon described is that

Figure 5 (Color online) Stress-strain curve of perfect α-Fe during stretching process.
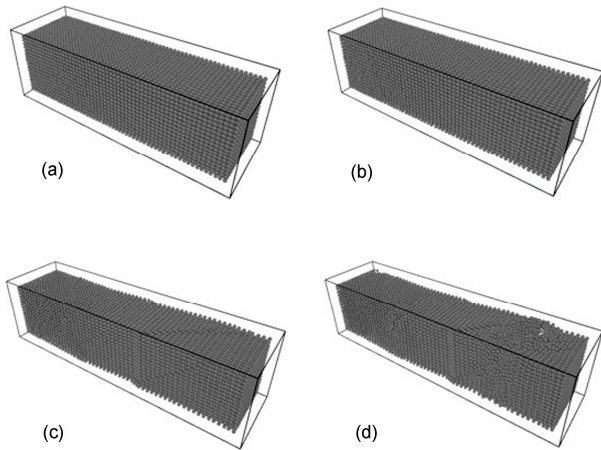
Figure 6   Schematic of stretching process. (a) Elastic deformation stage, (b) yield stage, (c) plastic deformation stage, and (d) ruptured.

the stress σ and strain ε maintain a linear relationship at the elastic deformation stage in accordance with Hooke's law, which is expressed as follows:

$$\sigma = E\varepsilon, \tag{7}$$

where E is the elastic modulus (also known as Young's modulus) that is numerically equal to the slope of the stress-strain curve at the elastic deformation stage. Since the model not only can be seen as a single crystal material but also can be loaded axially, the following equation can be established at the yield stage:

$$\tau = \sigma \cos \lambda \cos \phi, \tag{8}$$

where λ is the angle between the crystal slip direction and given force, φ is the angle between the normal slip plane and center axis, and τ is the shear stress on the slip direction. When the shear stress τ in eq. (8) reaches a critical value, the slip between the crystal planes begins, which corresponds to yield. Single crystal plastic deformation occurs because of the atom dislocation slip. The single crystal starts plastic deformation when the atoms stack along the stretch direction instead of staying in their original places under the effect of axial static tensile loading.

According to the data obtained by simulation, the average elastic modulus of perfect α-Fe along the [100] direction can be calculated as 168.6 GPa. Reflecting resistance to elastic deformation, elastic modulus is a key parameter to characterize the bond strength of atoms in the internal material. The greater its value, the more difficult the material deforms elastically. However, a closer look at Figure 5 shows that the slope of the curve, i.e., the elastic modulus, is not constant at the elastic deformation stage. To show the changes in the elastic modulus, Figure 7 illustrates a curve of elastic modulus versus elastic strain in the range of elastic deformation of perfect α-Fe obtained by derivation calculus of stress to strain. This figure also indicates that the

elastic modulus is not constant but decreases with the increase of strain during the elastic deformation stage. The variation may be due to the inhomogeneity of the cross-section of α-Fe during the tensile process, which results from the surface effect [27] and reduces the elastic modulus of the bulk until the yield stage to produce yield effects.

3.4   Point defect effect

The tensile stress–strain curve that corresponds to different point defect concentrations in α-Fe is shown in Figure 8. The shape of each tensile stress–strain curve has the same character as the shape of the defect-free α-Fe curve, which undergoes elastic deformation, yield, and plastic deformation until it finally fractures. All of the curves shown in Figure 8 exhibit a significant decline stage when the α-Fe model fractures. Thus, we have to pay attention to the aforementioned stages instead of studying the meaningless part of the curve after fracture.

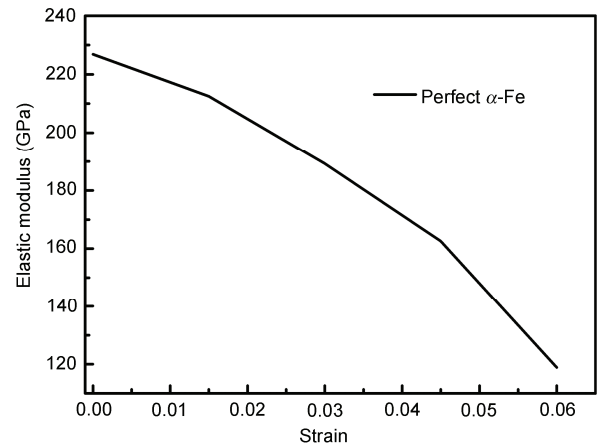By comparing the elastic deformation stage and yield

Figure 7   Curve of elastic modulus versus strain at elastic deformation stage of perfect α-Fe.
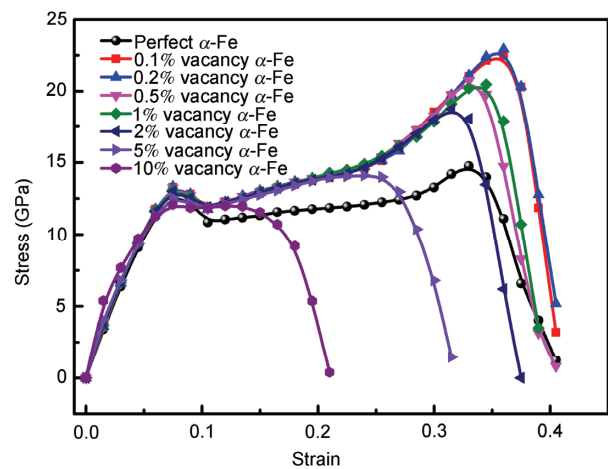

Figure 8   (Color online) Stress-strain curve of α-Fe with different vacancy concentrations during stretching process.

stage of each curve in Figure 8, we can observe that all these curves except the curve with 10% vacancy concentration almost overlap in the first two stages. This phenomenon results from atom migration during the relax and tensile process because minimal vacancies exist in the material with 5% or less vacancy concentration, thereby reducing the lattice distortion caused by vacancies. As a result, the elastic modulus and elastic limit have almost no difference. The large number of vacancies in the material, some of which may cluster into voids, result in ineffectiveness in reducing lattice distortion by atomic migration. Thus, the elastic modulus and elastic limit of the material with 10% vacancy concentration both decrease by 9.7% compared with the maximum elastic modulus and elastic limit shown in Figure 8.

Comparing the plastic deformation stage of all the curves reported in Figure 8, we have found that the curve with 10% vacancy concentration has no clear rising trend. The material maintains its yield stress horizontally at the initial plastic deformation stage, and then fractures after a certain deformation. The curve with 5% vacancy concentration also has no apparent ultimate tensile strength; it has a short rise and the material fractures immediately after the rise. As shown in Figure 8, however, the curves with different vacancy concentrations from 0.1% to 2% all have a clear upward process and fracture occurs at different strains when the ultimate tensile strength is reached. The ultimate tensile strengths in these five curves are presented in Figure 9. As this figure shows, with the increasing vacancy concentration, the ultimate tensile strength initially increases and then decreases after reaching the peak value of 22.9 GPa whose vacancy concentration is 0.2%. The reason for this phenomenon is easy to understand. Since the vacancy is produced as a defect, the dislocation, which is generated during the deformation process, is trapped by it. As a result, the movement of dislocation is blocked. Thus, the stress must be increased to make the dislocation move again, which causes the ultimate tensile strength to increase as shown in Figure 8. Nevertheless, this kind of effect becomes obvious only when the vacancy concentration is not extremely high, such as 0.1% and 0.2%. If the vacancy concentration exceeds the limits, it becomes counterproductive. As the concentration increases, vacancies could possibly form dislocation more easily, which results in less effectiveness in blocking the dislocation and the reduction of the ultimate tensile strength of the material.

4   Conclusion

In this study, simulations have been conducted to study the mechanism of the irradiation-induced vacancy formation in iron materials under neutron irradiation environment. Three commonly used structure materials are considered in terms of DDR distribution along with depth and non-ionizing contribution to the whole DDR. The results indicate that the
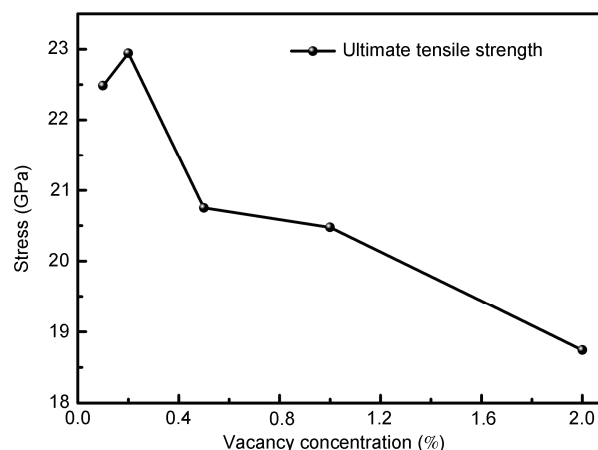
Figure 9   Ultimate tensile strength of α-Fe with five different kinds of vacancy concentration from 0.1% to 2.0%.

material damage caused by neutrons is mainly displacement damage, while the displacement damage rate and the non-ionizing effect of neutrons decrease with the increase of neutron energy. At the same time, the non-ionizing effect of neutrons also contributes significantly.

Objective laws on the effect of vacancy concentration on the mechanical properties of α-Fe have been investigated as well. After the simulation of the stretching process of α-Fe under the atomic scale, some valuable conclusions can be made. The elastic modulus, yield strength, and ultimate strength of α-Fe are in the order of magnitude of GPa. However, the elastic modulus is not constant but decreases with the increase of strain at the elastic deformation stage. The ultimate strength reaches its maximum when the vacancy concentration in α-Fe is 0.2%. On the basis of these findings, decreasing or increasing the number of vacancies reduces the ultimate strength.

1   Phythian W J, Stoller R E, Foreman A J E, et al. A comparison of displacement cascades in copper and iron by molecular dynamics and its application to microstructural evolution. J Nucl Mater, 1995, 223: 245–261

2   Yang Y H, Tang X B, Chen F D, et al. A molecular dynamics-based comparison of defect production in collision cascades during the bombardment of iron with different ions. Sci China Tech Sci, 2014, 57: 29–34

3   Grimes R W, Nuttall W J. Generating the option of a two-stage nuclear renaissance. Science, 2010, 329: 799–803

4   Grimes R W, Konings R J M, Edwards L. Greater tolerance for nuclear materials. Nat Mater, 2008, 7: 683–685

5   Liu X Y, Uberuaga B P, Demkowicz M J, et al. Mechanism for recombination of radiation-induced point defects at interphase bounda-

ries. Phys Rev B, 2012, 85: 012103

6 O'Brien M H, Loughlin M J. Displacement damage quantification in future fusion systems. Fusion Eng Des, 2007, 82: 2536–2542

7 Huang H, Tang X, Chen F, et al. Radiation damage resistance and interface stability of copper–graphene nanolayered composite. J Nucl Mater, 2015, 460: 16–22

8 Chen F, Tang X, Yang Y, et al. Investigation of structural stability and magnetic properties of Fe/Ni multilayers irradiated by 300 keV Fe[10+]. J Nucl Mater, 2014, 452: 31–36

9 Alamo A, Bertin J L, Shamardin V K, et al. Mechanical properties of 9Cr martensitic steels and ODS-FeCr alloys after neutron irradiation at 325 °C up to 42 dpa. J Nucl Mater, 2007, 367: 54–59

10 Nagai Y, Tang Z, Hassegawa M, et al. Irradiation-induced Cu aggregations in Fe: An origin of embrittlement of reactor pressure vessel steels. Phys Rev B, 2001, 63: 134110

11 Nishiyama Y, Onizawa K, Suzuki M, et al. Effects of neutron-irradiation-induced intergranular phosphorus segregation and hardening on embrittlement in reactor pressure vessel steels. Acta Mater, 2008, 56: 4510–4521

12 Garner F A, Toloczko M B, Sencer B H. Comparison of swelling and irradiation creep behavior of fcc-austenitic and bcc-ferritic/martensitic alloys at high neutron exposure. J Nucl Mater, 2000, 276: 123–142

13 Konobeev Y V, Dvoriashin A M, Porollo S I, et al. Swelling and microstructure of pure Fe and Fe–Cr alloys after neutron irradiation to∼ 26 dpa at 400 °C. J Nucl Mater, 2006, 355: 124–130

14 Gilbert M R, Dudarev S L, Zheng S, et al. An integrated model for materials in a fusion power plant: transmutation, gas production, and helium embrittlement under neutron irradiation. Nucl Fusion, 2012, 52: 083019

15 Barashenkov V S. Monte Carlo simulation of ionization and nuclear processes initiated by hadron and ion beams in media. Comput PhysCommun, 2000, 126: 28–31

16 Osetsky Y N, Bacon D J. Atomic-scale modelling of primary damage and properties of radiation defects in metals. Nucl Instrum Meth B, 2003, 202: 31–43

17 Osetsky Y N, Bacon D J, Serra A, et al. Stability and mobility of defect clusters and dislocation loops in metals. J Nucl Mater, 2000, 276: 65–77

18 Caturla M J, Soneda N, Alonso E, et al. Comparative study of radiation damage accumulation in Cu and Fe. J Nucl Mater, 2000, 276: 13–21

19 Agostinelli S, Allison J, Amako K, et al. GEANT4—A simulation toolkit. Nucl Instrum Meth A, 2003, 506: 250–303

20 Norgett M J, Robinson M T, Torrens I M. A proposed method of calculating displacement dose rates. Nucl Eng Des, 1975, 33: 50–54

21 Kinchin G H, Pease R S. The displacement of atoms in solids by radiation. Rep Prog Phys, 1955, 18: 1

22 Ackland G J, Bacon D J, Calder A F, et al. Computer simulation of point defect properties in dilute Fe–Cu alloy using a many-body interatomic potential. Philos Mag, 1997, 75: 713–732

23 Andersen H C. Molecular dynamics simulations at constant pressure and/or temperature. J Chem Phys, 1980, 72: 2384–2393

24 Nosé S. A unified formulation of the constant temperature molecular dynamics methods. J Chem Phys, 1984, 81: 511–519

25 Berendsen H J C, Postma J P M, van Gunsteren W F, et al. Molecular dynamics with coupling to an external bath. J Chem Phys, 1984, 81: 3684–3690

26 Plimpton S. Fast parallel algorithms for short-range molecular dynamics. J Comput Phys, 1995, 117: 1–19

27 Wu H A. Molecular dynamics study on mechanics of metal nanowire. Mech Res Commun, 2006, 33: 9–16